Article:
Edwards, S.M. orcid.org/0000-0001-5011-4688, Harding, A.L., Leedale, J.A. et al. (4 more authors) (2024) An advanced in silico model of the oral mucosa reveals the impact of extracellular spaces on chemical permeation. International Journal of Pharmaceutics, 666. 124827. ISSN 0378-5173

https://doi.org/10.1016/j.ijpharm.2024.124827

International Journal of Pharmaceutics 666 (2024) 124827

Contents lists available at ScienceDirect

International Journal of Pharmaceutics

journal homepage: www.elsevier.com/locate/ijpharm

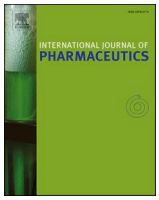

An advanced *in silico* model of the oral mucosa reveals the impact of extracellular spaces on chemical permeation

Sean M. Edwards [a,1], Amy L. Harding [b,1], Joseph A. Leedale [c], Steve D. Webb [c], Helen E. Colley [b], Craig Murdoch [b,1,*], Rachel N. Bearon [a,d,2,*]

[a] Department of Mathematical Sciences, University of Liverpool, Liverpool L69 7ZL, United Kingdom
[b] School of Clinical Dentistry, University of Sheffield, Sheffield S10 2TA, United Kingdom
[c] Syngenta, Jealott's Hill International Research Centre, Bracknell RG42 6EY, United Kingdom
[d] Department of Mathematics, King's College London, London WC2R 2LS, United Kingdom

ARTICLE INFO

Keywords:
Mathematical modelling
In silico
Drug delivery
Oral mucosa
Toxicology
Permeation
Systems pharmacology
Chemical toxicity

ABSTRACT

Accurately predicting the permeation of chemicals through human epithelial tissues is crucial for pharmaceutical therapeutic design and toxicology. Current mathematical models of multi-layered stratified squamous epithelium such as those in the oral cavity use simplistic 'bricks and mortar' geometries that do not fully account for the complex cellular architecture that may affect chemical permeation in these tissues. Here we aimed to develop a new, advanced mechanistic mathematical model of the human epithelium that more accurately represents chemical tissue permeation. Using measurements of cell size and tortuosity from micrograph images of both human oral (buccal) and tissue-engineered buccal mucosa along with mechanistic mathematical modelling, we show that the convoluted geometry of the extracellular spaces within the epithelium significantly impacts chemical permeation. We next developed an advanced histologically and physiologically-relevant *in silico* model of buccal mucosal chemical permeation using partial differential equations, fitted to chemical permeation from *in vitro* assay data derived from tissue-engineered buccal mucosal models and chemicals with known physiochemical properties. Our novel *in silico* model can predict epithelial permeation kinetics for chemicals with different physicochemical properties in the absence or presence of permeability enhancers. This *in vitro* – *in silico* approach constitutes a step-change in the modelling of chemical tissue permeation and has the potential to expedite pharmaceutical innovation by improved and more rapid screening of chemical entities whilst reducing the need for *in vivo* animal experiments.

1. Introduction

The oral mucosa (the tissue lining the oral cavity) is now recognized as an attractive drug delivery site as an alternative to injection and oral administration. It offers an array of benefits such as being non-invasive, avoidance of first-pass metabolism by the liver, practicality of administration and increased patient compliance (Targhotra and Chauhan, 2020). The buccal (cheek) mucosa is a particularly suitable site for drug delivery because it is composed of a non-keratinized epithelium that is several-times more permeable than the skin and, along with its highly vascularized underlying connective tissue, promotes rapid chemical absorption that is integral for effective topical or systemic drug delivery (Hearnden et al., 2012). Currently, only a small number of chemicals are routinely delivered via the oral mucosa for systemic applications (e.g., glyceryl trinitrate for angina, fentanyl citrate for pain, and prochlorperazine for nausea). However, the development of advanced polymer-based manufacturing technologies for mucoadhesive patches and other smart intraoral systems have marked a substantial step forward in this drug delivery domain (Edmans et al., 2020; Zhou et al., 2022). It is projected that these emerging technologies will drive a significant expansion in the catalogue of pharmaceutical compounds available for administration through the oral mucosa (Colley et al., 2018; Edmans et al., 2020). For example, clinical trials have been undertaken for administration of patch-containing corticosteroids for the

* Corresponding authors.
E-mail address: c.murdoch@sheffield.ac.uk (C. Murdoch).
[1] Authors contributed equally to this work. *Joint senior and corresponding authors.
[2] Present address: RNB's affiliation is now Kings College London, United Kingdom.

https://doi.org/10.1016/j.ijpharm.2024.124827
Received 28 April 2024; Received in revised form 25 September 2024; Accepted 11 October 2024
Available online 14 October 2024

treatment of inflammatory oral lesions (Brennan et al., 2022; Ibrahim et al., 2023). As the scope of compounds likely to be delivered via the mucosa expands, it is imperative for future drug screening and chemical toxicity testing that robust *in vitro-in silico* correlation models are established that accurately predict chemical performance *in vivo*. The integration of these models will expedite the translation of chemical formulations from *in vitro* testing to full-scale commercial production, while simultaneously reducing the requirement for animal experiments during the pre-clinical phase.

In silico modelling of drug/chemical permeation through human tissues is highly advantageous for the development of novel pharmaceutics and toxicological screening. The current *in silico* predictive approaches for epithelial tissues are empirical models that directly fit permeation rates to the biophysical properties of a chemical (Goswami et al., 2013; Kokate et al., 2009), compartmental analysis with well-mixed homogeneous tissue layers (Kruse et al., 2007; Polak et al., 2012; Xia, 2015) or approximate diffusive models that are based on 'brick and mortar' cellular geometries (Chen et al., 2015; Verma et al., 2023). These models do not take into account the complex tissue structure of the buccal epithelium and ignore the spaces that exist between cells (extracellular spaces), which then underrepresents chemical permeation via the paracellular route. Alternatively, the microscale geometry of a tissue can be included by using partial differential equations (PDEs). Such models can elucidate the impact of microscale factors such as cellular geometry, permeation of cell membranes and cell metabolism, which varies depending on a chemical's properties. A cell-based approach of this type was recently established in liver spheroids (Leedale et al., 2020), which allowed for extracellular and intracellular predictions and consideration of paracellular permeation. Herein, we aimed to develop a new, advanced mechanistic mathematical model of the human epithelium that more accurately represents chemical tissue permeation.

The development and use of tissue engineered three-dimensional models of human epithelium such as skin and the oral mucosa has expanded exponentially in recent years (Kinikoglu et al., 2015; Klausner et al., 2021; Moharamzadeh et al., 2012). Their increased use has been driven by the low availability of human tissue for research (which is particularly acute for oral mucosal tissue), the desire to move away from the use of animals in experiments and the realization that the structure and molecular constituents of animal and human tissue is often different. We and others have previously shown that tissue engineered models of the normal human oral mucosa (TENOM) have very similar histological structure and express the same key cellular and tissue markers (cytokeratins, desmosomes, tight junctions, hemidesmosomes) as native human oral mucosa (Buskermolen et al., 2016; Gibbs and Ponec, 2000; Jennings et al., 2016; Said et al., 2021). These *in vitro* models also have similar transepithelial chemical permeability profiles as porcine buccal mucosa (Bierbaumer et al., 2018; Boateng and Okeke, 2019; De Caro et al., 2008; Giannola et al., 2007; Rai et al., 2011), the main animal tissue used to represent the human oral mucosa in research, making TENOM suitable tissue surrrogates.

In this study, the microscale structure of the oral buccal epithelium was investigated to understand the mechanisms behind chemical permeation through this tissue. For the first time, we quantify the extracellular space on a subcellular scale and measure the tortuosity in the buccal epithelium of both human normal oral mucosa (NOM) and TENOM. These data inform an innovative *in silico* model of chemical permeation through the buccal mucosa, which incorporates the histological structure of the epithelium. We demonstrate the importance of cellular tortuosity within the mucosa upon validation of the model with the clinically used chemicals: doxorubicin hydrochloride (HCl), oxymetazoline HCL, and clobetasol-17-propionate. The data generated from investigations of chemical permeation *in vitro* using TENOM, parameterized and extrapolated to an advanced *in silico* model, provide a more comprehensive understanding of the impact that subcellular structures have on buccal mucosal drug delivery. This *in silico* model represents a step-change in modelling chemical permeation, the principles of which could be extrapolated to assess chemical permeation *in vivo* or in other epithelial tissues.

2. Materials amd Methods

All reagents were purchased from Merck (Gillingham, United Kingdom) and used as per the manufacturers' instructions unless otherwise stated.

2.1. Oral tissue and tissue-engineered normal oral mucosal (TENOM) models

TENOM were constructed as previously described (Jennings et al., 2016) using TERT-immortalized oral keratinocytes (FNB6) originally isolated from a female buccal mucosal biopsy (McGregor et al., 2002) and NOF, isolated from the freshly excised buccal mucosa of a 26-year old, non-smoking female (with written, informed consent, UK Research Ethical Approval number 09/H1308/66) following enzyme digestion, as previously described (Colley et al., 2011).

2.2. Histological image analysis

Normal oral mucosal (NOM) was sourced from freshly excised buccal tissue from healthy volunteers (female aged 31, female aged 24 and male aged 46, all non-smokers) with written, informed consent (UK Research Ethical Approval number 09/H1308/66) and along with TENOM were fixed with 10 % (v/v) neutral-buffered formalin, processed, paraffin wax-embedded, 5 μm sections cut using a microtome and sections stained with haematoxylin & eosin (Epredia, UK). Slides were mounted with distyrene-polystrene xylene and imaged by light microscopy. Images were digitised using an Aperio Slide Scanner (Leica) and extracellular space widths measured using the associated Aperio ImageScope software (Leica Biosystems, UK) or ImageJ software (NIH).

2.3. Extracellular space analysis using transmission electron microscopy

NOM biopsies and TENOM were fixed with 3 % glutaraldehyde diluted in 0.1 M cacodylate buffer (pH 7.4) for 2 h at 4 °C before rinsing twice in 0.1 M phosphate buffer (pH 7.4) at 4 °C. Samples were subjected to post-fixation, dehydration and resin embedding as described previously (Said et al., 2021). Sections were examined for extracellular spaces using an FEI Tecnai transmission electron microscope (TEM) at an accelerating voltage of 80 kV and images taken using a Gatan digital camera. Post-image measurements were conducted on the convoluted extracellular spaces by assuming that they are locally sinusoidal with width w, amplitude A and wavelength λ. Measurements were collected for basal, spinosum and superficial epithelial strata. Extracellular space widths were measured using ImageJ software (NIH).

2.4. Buccal mucosa chemical permeation assay using TENOM

Chemical permeation of buccal mucosa was performed using a transwell tissue culture system where TENOM were cultured on 0.4 μm pore permeable membranes. A schematic of this assay design is shown in Fig. 4A. Here, the buccal epithelial surface was exposed to the air, mimicking the situation *in vivo*, while the apical side of the connective tissue was in contact with the basolateral receiver chamber that contained 2 mL of receptive solution (PBS, pH 7.4). A constant environment of 37 °C, 5 % CO_2 in a humidified incubator was maintained throughout the experiment to mimic physiological conditions. TENOM were equilibrated with pre-warmed receptive solution for 15 min before addition of 50 μL of the chemical (1 mg/mL made up in PBS): doxorubicin HCl [1.72 mM, logP = 0.97], clobetasol-17-propionate [2.14 mM, logP = 3.84] and oxymetazoline HCL [3.4 mM, logP = 3.37] that were each topically applied to the apical surface of the epithelium. All these

chemicals are soluble in PBS at the concentrations used. Permeation of chemicals across the buccal mucosa was determined by collecting 200 μL aliquots from the receiver chamber at 0.5, 1, 2, 3, 4, 5, 6 and 24 h with 200 μL fresh pre-warmed PBS immediately added back to the receiver chamber each time point to maintain experimental conditions. The level of chemical permeating through the TENOM was determined using high performance liquid chromatography (HPLC) where chemical concentrations were interpolated from standard calibration curves. The percentage permeated was calculated at each (n^{th}) timepoint from concentrations C using

$$\%_{\text{permeated}}(n) = 100 \times \left[\frac{V_{receiver}C_n + V_{aliquot}(C_1 + C_2 + \cdots C_{n-1})}{V_{applied}C_{applied}}\right], \quad (1)$$

with applied, receiver and aliquot volumes $V_{applied} = 50$ μL, $V_{receiver} = 2$ mL, $V_{aliquot} = 200$ μL and applied concentration $C_{applied} = 1$ mg/mL. Eq. (1) is derived from conservation of mass using standard molar relations and accounts for the small removal of chemical with each aliquot taken. All permeation experiments were performed on three separate occasions for each chemical and HPLC runs for each individual sample were done in triplicate.

2.5. High-performance liquid chromatography

HPLC analytical grade chemicals and reagents were used for all experiments (Merck, UK). Oxymetazoline-HCL [1 mg/mL] and doxorubicin-HCL [1 mg/mL] in PBS pH 7.4 and clobetasol-17-propionate [1 mg/mL] in methanol were initially analysed for detection wavelengths and absorbance spectra using parameters observed in the following publications (Said et al., 2021; Shah et al., 2018; Stanisz and Nowinski, 2000). The phase conditions were further optimised and validated for each chemical compound. Detection was performed using a Shimadzu prominence HPLC with UV/Vis detection. A XBridge BEH-C18 (4.6 mm × 250 mm), 130 Å pore size column was used throughout. Oxy-HCL mobile phase consisted of MeCN (40 %)/ KH_2PO_4 in 0.1 % $H_3(PO)_4$ (60 %) with 10-minute runs and column eluent monitored at 280 nm. Doxorubicin required a gradient method for detection consisting of a mobile phase of 50 mM (KH_2PO_4 + 0.1 % phosphoric acid) + (MeCN) (0:40 % − 7 min, 60:40 % − 7–10 min and 75:25 % − 12–15 min), with detection at 485 nm. For clobetasol-17-propionate, the mobile phase was composed of MeCN:H_2O 70:30 % v/v with emission detected at 239 nm in 10 min runs. All samples had an injection volume of 20 μL and a flow rate of 1 mL min^{-1}, with readings taken at 20 °C.

For HPLC validation, each chemical was solubilised to a stock solution. Standard solutions of each chemical were prepared by further dilution with HPLC grade water. For oxymetazoline-HCL the concentration of detection ranged from 1- 40 μg/mL [16.9–673.8 μM], for doxorubicin-HCL this was 1–50 μg/mL [8.6–431.1 μM] while clobetasol-17-propionate was detectable in the range of 1–25 μg/mL [10.7–267.7 μM]. Linear regressions were generated and the slope, intercept and correlation coefficient plotted for each standard curve calculated. All calibration measurements were conducted in triplicate and a correlation coefficient of 0.99 was obtained for each chemical. Regression statistics were calculated for the lower limit of detection (LoD) and limit of quantification (LoQ) from results of calibration curves. These are defined as the concentration of analytes with a signal-to-noise ratio of 3:1 and 10:1, respectively, and are calculated using the following equations: LoD = ($3.3\sigma/s$) and LoQ= ($10\sigma/s$), where σ is the standard deviation of intercept and s is the slope of the calibration plot (Table S1).

2.6. Data analysis

All data are presented as mean ± SD, with all experimental repeats clearly stated. Data was analysed by ordinary one-way ANOVA with Tukey's post-hoc test for multiple group comparisons. Statistical analysis was performed using GraphPad prism, version GraphPad Prism version 10.0.0 (GraphPad Software, Boston, Massachusetts, USA) and significance assumed if $p < 0.05$.

2.7. Tortuosity calculations

Subcellular tortuosity τ_S of convoluted gaps is the sinusoidal path-length compared to the wavelength (Fig. 1F, Table S2),

$$\tau_S = \frac{1}{\lambda}\int_0^{\lambda}\left[1 + \left(\frac{2\pi A}{\lambda}cos\left(\frac{2\pi\widetilde{x}}{\lambda}\right)\right)^2\right]^{1/2} d\widetilde{x}, \quad (2)$$

Cellular tortuosity $\tau_C = (h+b)/h$ (Table S2) is approximated from the height h and breadth b of cells (Fig. 1G, Table S3). The overall tortuosity of the tissue $\tau = \tau_C\tau_S$ (Table S2) is a combination of these contributions.

2.8. In silico model of chemical permeation through an oral epithelial monolayer

The *in silico* monolayer model (Fig. S1A) has rectangular cells mimicking a buccal mucosal basal layer; cell breadth b (aligned with x) and height h (aligned with y) match NOM experimental measurements. The domain has a vertical extracellular gap (width w) and horizontal gaps above and below the cell-layer (widths $w/2$). Extracellular spaces between cells are sinusoidal, approximating experimental measurements (Fig. 1E). Chemicals diffuse through the extracellular and intracellular regions (coefficients D_E, D_I) with concentrations (C_E, C_I),

$$\frac{\partial C_E}{\partial t} = D_E\nabla^2 C_E, \frac{\partial C_I}{\partial t} = D_I\nabla^2 C_I. \quad (3)$$

Passive transport of chemical through cell boundaries is modelled with a permeability coefficient Q,

$$D_E\nabla C_E\cdot\boldsymbol{n} = D_I\nabla C_I\cdot\boldsymbol{n} = Q(C_E - C_I), \quad (4)$$

with flux conserved; a full discussion is given in (Leedale et al., 2020). A constant supply of chemical with concentration C_0 is applied at the top and a perfect sink mimics vascular uptake at the bottom,

$$C_E(y=0) = C_E(y = H+w) - C_0 = 0. \quad (5)$$

Each cell has the same concentration profile with symmetry on the side boundaries,

$$\frac{\partial C_E}{\partial x}(x=0) = \frac{\partial C_I}{\partial x}(x=0) = \frac{\partial C_E}{\partial x}(x = W+w) = \frac{\partial C_I}{\partial x}(x = W+w) = 0. \quad (6)$$

2.9. In silico model of chemical permeation through tissue-engineered normal oral mucosa

Cell nuclei coordinates inferred from stained tissue sections (Fig. 3B) were used to generate cells via Voronoi tessellation (Fig. 3C, see (Kaliman et al., 2016)). Cell elongation from the basal to the superficial layer (Fig. 1) is captured by adjusting the metric such that the distance d between two points $p_0(x_0, y_0)$ and $p_1(x_1, y_1)$ is,

$$d(p_0, p_1) = \left[(x_1 - x_0)^2 + \beta^2(y_1 - y_0)^2\right]^{1/2}, \quad (7)$$

with elongation parameter $\beta = h/b$ ($\beta = 1$ is Euclidean and $\beta > 1$ cells were elongated in the x coordinate). Elongation β is assumed to increase linearly throughout the epithelium. To the authors knowledge this is the first time elongated Voronoi tessellation has been applied *in silico* (cell elongation is common in other tissues (Lemke and Nelson, 2021)); though this approach has been discussed theoretically (Chen et al., 2019). Extracellular spaces were imposed with the polygon offset algorithm with gap widths w. There is no loss by evaporation or to the

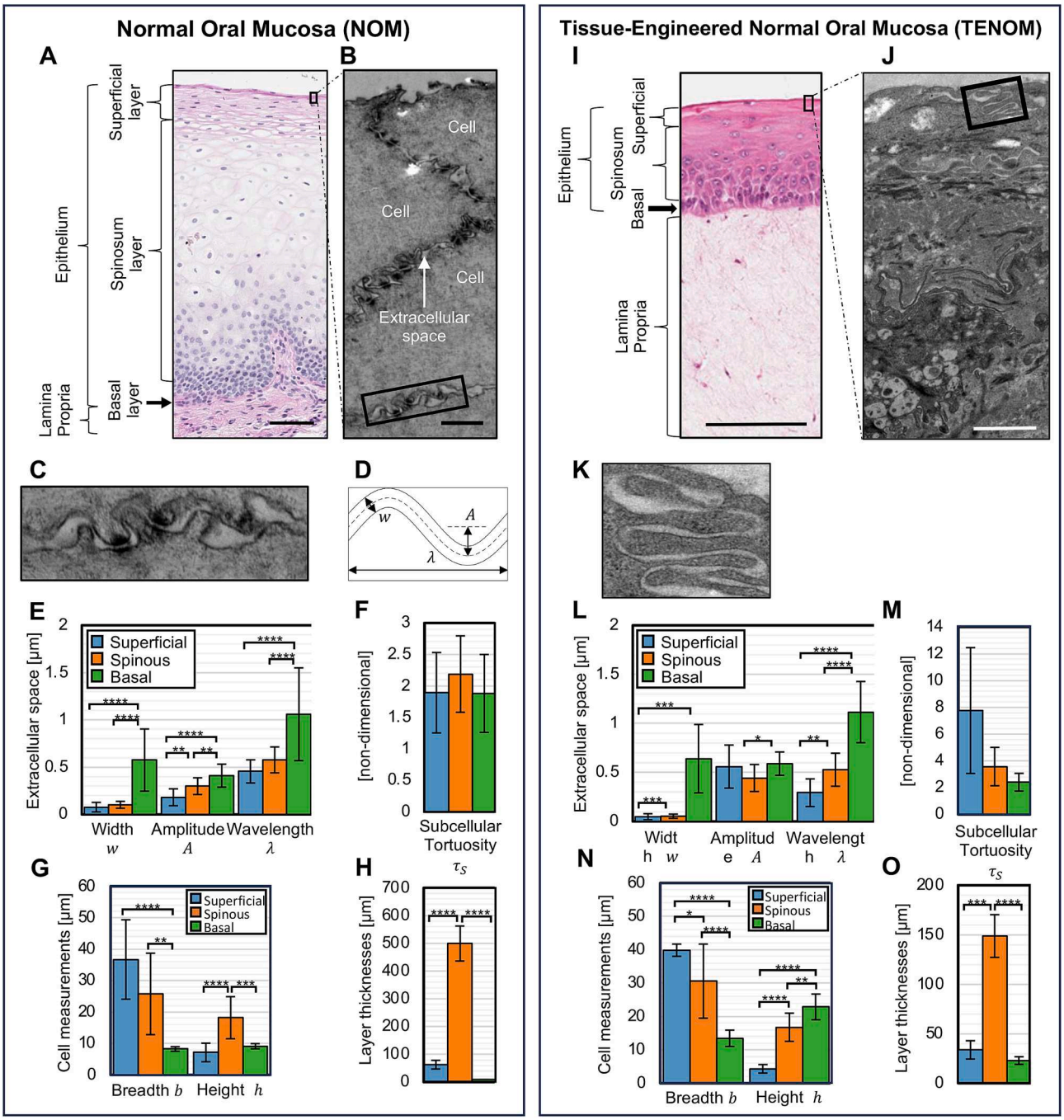

Fig. 1. Quantification of extracellular space convolutions and tissue geometry on the subcellular scale in the oral mucosa. (A) Histological section of a normal oral mucosal biopsy displaying distinct cell layers, scale bar = 100 μm. (B) Transmission electron micrograph images of cells in the superficial layer displaying convoluted extracellular spaces between cells on a subcellular scale, scale bar = 1 μm. (C) Magnified image of convoluted extracellular spaces in B reveals a quasi-periodic profile of extracellular spaces. (D) Schematic of the extracellular space convolutions, assuming a sinusoidal profile with space width w, amplitude A and wavelength λ. (E) Measurements of extracellular space width, amplitudes and wavelengths and (F) subcellular tortuosity in each oral epithelial strata of normal oral mucosa (NOM), legend in (E) applies to (F,G,H). (G) Cell breadth and height, and (H) cell layer thicknesses measured in each strata. (I-O) Tissue-engineered normal oral mucosa measurements for comparison. Data is expressed as mean ± SD., * $p < 0.05$, ** $p < 0.01$, *** $p < 0.001$ and **** $p < 0.0001$ as analyzed by ordinary one-way ANOVA with Tukey's correction (n = 3 independent biopsies with at least 10 measurements taken from each image).

mouth and diffusion in each layer is modelled as before (e.g., Eqn. (3). Along the boundaries between layers flux is conserved; cell membrane permeation is modelled by Eqn. (4).

2.10. Solving the in silico models numerically

Diffusion equations (Eqn. (3)) were solved in each region subject to (Eqns. 4–6) with a finite-element scheme and time-stepping with the Crank-Nicolson method. Three initial implicit-Euler steps were taken to accommodate discontinuous initial conditions. The numerical schemes were solved using EpiPerm, our purpose-built C++ library which models epithelial permeation, and the linear solve phase was undertaken with the parallel sparse solver MUMPS (Amestoy et al., 2001) under the framework of PETSc (Balay et al., 1997). Initially, the numerical meshes were constructed in MATLAB and then refined with EpiPerm. Solutions are ensured to be independent of discretization.

Average concentrations are computed by integrating over a relevant region and dividing by its area.

2.11. Parameterizing the in silico model to capture permeation of chemicals

Diffusion in the application D_A and lamina propria D_{LP} layers was approximated to water D_W, determined with the Stokes-Einstein equation (Miller, 1924) for a given chemical,

$$D_A = D_{LP} = D_E{\tau_S}^2 = D_W = \frac{k_B T}{6\pi\eta_W R} \tag{8}$$

with Boltzmann constant $k_B = 1.38065 \times 10^{-23}$ m^2 kg s^{-2} K^{-1}, physiological temperature $T = 310.15K$, dynamic viscosity of water $\eta_W = 6.913 \times 10^{-4}$ kg m^{-1} s^{-1}, and spherical chemical radius R. Extracellular diffusion D_E is reduced to account for subcellular convoluted tortuosity ($\tau_S = 3.576$ for TENOM spinous layer, Table S3). The chemical radius is inferred with,

$$R = \left(\frac{3M}{4\pi N_A \rho}\right)^{1/3}, \tag{9}$$

with Avagadro's constant $N_A = 6.0221 \times 10^{23}$, chemical molecular mass M and density ρ. Diffusion in the intracellular D_I and superficial D_S regions is reduced through the presence of organelles, which depends on the size of the chemical. We adopt the model suggested by Kwapiszewska *et al.*, for human epithelial cell lines (Kwapiszewska et al., 2020),

$$D_I = D_S = \frac{D_W}{1.3}\exp\left[\left(\frac{\left(4.6\times10^{-9}\right)^2}{20^2} + \frac{\left(4.6\times10^{-9}\right)^{-2}}{R^2}\right)^{-0.285}\right]^{-1}. \tag{10}$$

To fit the predicted percentage permeated $P(Q,t)$ to *in vitro* permeation data, the cell membrane permeability Q is Newton iterated until the difference between the two curves is minimised in the L2 norm. Biochemical properties, diffusion coefficients and membrane permeability parameters for each chemical are listed in Table S4.

3. Results

3.1. Oral epithelium displays a convoluted extracellular space topology

The oral buccal mucosal epithelium is non-keratinized and therefore divided into three distinct layers characterized by cellular differentiation. Basal cells attach to the basement membrane of the connective tissue (lamina propria) and display a stem cell-like phenotype. Moving apically, the basal cells differentiate into the spinosum layer, where cells are larger in size, and finally into the superficial layer, where the terminally differentiated cells are thin and flat (Fig. 1A). Transmission electron micrographs show that the extracellular spaces between epithelial cells are convoluted and heterogeneous, differing in each epithelial strata (Fig. 1B-D). Whilst this has been observed in other tissues (e.g., skin (Vela-Romera et al., 2019)) this is the first time it has been measured and characterized in this manner for oral epithelium. In NOM, the superficial and spinous strata display a significantly narrower extracellular space with convolutions of lower amplitude and wavelength than the basal cells (Fig. 1E, $p < 0.01$), increasing cellular surface area and lengthening the extracellular path around cells that may restrict paracellular chemical permeation. Similar data is observed for the TENOM (Fig. I-M), evidencing the structural similarity between human biopsy and *in vitro* engineered buccal mucosa. From the basal to the superficial layer, the amplitude and wavelength of the convoluted spaces decrease, which individually affect tortuosity in opposing directions. The net effect of this is that the subcellular tortuosity τ_S, (i.e., the extracellular pathlength divided by the straight pathlength (Fig. S1C)), is similar throughout the epithelium with $\tau_S > 1$ (Fig. 1F and M).

The height and breadth of cells in each stratum along with the thickness of each stratum of the buccal epithelium were also measured (Fig. 1G-H and N-O). As cells differentiate from the basal to the superficial layer their breadth increases resulting in cellular elongation and characteristic flattening. This corresponds to increased tortuosity on a cellular scale as cells differentiate apically ('cellular tortuosity', Table S2), and the overall oral mucosal tortuosity τ (the product of subcellular and cellular tortuosities) also follows this trend (Table S2). A comparison between NOM and TENOM show that the basal and superficial strata display similar characteristics while the spinous stratum thicknesses is significantly increased in NOM compared to TENOM ($p < 0.0001$) (Fig. 1H and 1O). All data values are provided in Table S3.

3.2. Convoluted extracellular spaces affect chemical permeation dynamics

A physically-relevant *in silico* model of a basal cell monolayer, with discrete cells and extracellular spaces, was used to investigate the impact of convoluted extracellular space on chemical permeation into and around cells. A schematic of this model is shown in Fig. S1A, with convoluted geometry based on experimental measurements from NOM (Fig. 1E-G). A constant supply of chemical is applied at the apical cell surface with concentration C_0 (from time $t = 0$ *s*) and below the cells a perfect sink ($C = 0$) mimics chemical delivery to the lamina propria or vascular uptake. This approximation is suitable for basal cells which lie near to the lamina propria, but the same system can also be used to study the effect of convoluted gaps in the superficial and spinous strata if the breadth and height of cells along with convoluted extracellular space measurements are adjusted appropriately. A test chemical is applied with extracellular and intracellular diffusion coefficients $D_E = D_I = 7.5$ x 10^{-10} m^{2}s^{-1}. In practice, the diffusion coefficient depends on the physicochemical properties but previous analysis of the diffusion coefficients of over three hundred small molecule chemicals has suggested that this is reasonable as a representative value (Leedale et al., 2020).

Including the convoluted extracellular space makes substantial and predictable changes to chemical permeation dynamics, and the *in silico* model can also predict variability across different epithelial strata. This is illustrated in Fig. 2 for three example chemicals each with differing ability to passively permeate the cell membrane, thereby mimicking highly membrane-permeating chemicals (Fig. 2A), moderately membrane-permeating chemicals (Fig. 2B) or membrane impermeable chemicals (Fig. 2C). Here, the chemical's membrane permeability (coefficient Q) is dependent on multiple physicochemical properties, including lipophilicity (logP), molecular mass and ionization that each affect Q in a non-linear manner. As a constant supply of chemical is applied, the system reaches a steady-state (Fig. 2Ai–Ci). Average concentrations over time are deduced in the extracellular space between cells (Fig. 2Aii–Cii) and intracellularly, within the cell (Fig. 2Aiii–Biii).

The membrane permeability of a chemical alters its intra and extracellular dynamics. For highly membrane-permeating chemicals (Fig. 2Ai, $Q = 10^{-3}$ ms^{-1}), the average chemical concentrations in the extracellular space (Fig. 2Aii) and intracellularly (Fig. 2Aiii) are identical, indicating that the geometry of the extracellular space has little impact on permeation. Here, permeation through the monolayer is governed by diffusion, with diffusion time increasing monotonically with cell height h (Fig. 1G). However, moderately membrane-permeating chemicals have a different steady-state profile intra- and extracellularly (Fig. 2Bi, $Q = 10^{-5}$ ms^{-1}). The time to reach steady-state is significantly slower in both regions (Fig. 2Bii, 2Biii), with extracellular space and intracellular concentrations remaining coupled. In contrast to membrane-permeating chemicals, the time to reach steady-state is no longer in order of cell height, indicating the influence of other geometric factors including subcellular tortuosity or cell area. Membrane impermeable chemicals ($Q = 0$), are restricted to the

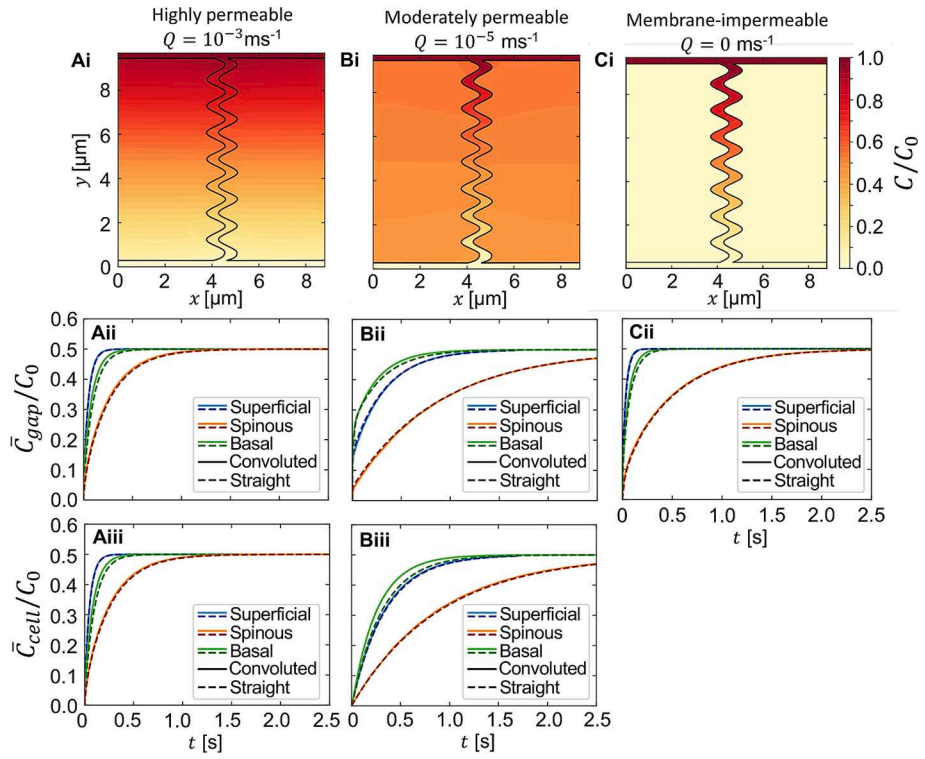

Fig. 2. Chemical permeation through a monolayer of oral epithelial cells modelled *in silico*. A constant supply of chemical (concentration C_0) is passively transported through permeable membranes. Vascular uptake at the bottom is modelled by a perfect sink. Chemicals diffuse in the extra- and intracellular regions (coefficients $D_E = D_I = 7.5 \times 10^{-10}$ m^{2}s^{-1}). The physiochemical property of each model chemical Q is varied: (A) highly membrane-permeable $Q = 10^{-3}$ ms^{-1}; (B) moderately membrane-permeable $Q = 10^{-5}$ ms^{-1}; and (C) membrane-impermeable $Q = 0$ ms^{-1}. The concentration profile at steady state is presented (Ai, Bi, Ci) alongside average concentrations over time in the central extracellular space (Aii, Bii, Cii) and intracellularly (Aiii, Biii). Each type of epithelial cell strata is modelled (superficial, spinous, basal) in the full convoluted model (solid line) and results are compared with a straight approximation (dashed line) that has reduced extracellular diffusion (Eqn. (11).

membrane lipid bilayer or extracellular space and chemical permeation dynamics are dominated by transit along the convoluted paracellular route (Fig. 2Ci). The subcellular tortuosity of the extracellular space increases the length-scale for diffusion relative to membrane-permeating chemicals, thus increasing the time to reach steady-state in the extracellular space (Fig. 2Cii). However, this process is non-linear as the timescale to reach steady-state is faster than for moderately membrane-permeating chemicals. Further analysis of low membrane-permeating chemicals ($Q < 10^{-6}$ ms^{-1}) suggests that they are largely restricted to the extracellular space or plasma membrane with low permeation into cells over time (Fig. S2).

3.3. Reduced extracellular diffusion approximates effect of convoluted topology in silico

When compared against a straight extracellular space model in which the convoluted subcellular geometry has been removed, permeation through the monolayer is slower for the convoluted gaps than for the straight gaps (Fig. S3). However, an equivalence can be found if we introduce a slower effective diffusion coefficient for the straight gaps,

$$D_E^{straight} = \frac{D_E}{\tau_S^2}. \quad (11)$$

By appropriately slowing extracellular diffusion in the 'straight' extracellular space model (Fig. S1B) to incorporate the subcellular tortuosity of spaces (Eqn. (11)), the permeation dynamics of the physically relevant 'convoluted' cell monolayer are captured, particularly for spinous and superficial cells. This approximation can be applied in more sophisticated *in silico* models involving multiple cells for which the computational cost of incorporating the subcellular geometry would be prohibitive. If subcellular tortuosity is ignored there will be a consistent underestimation of the permeation timescales (Fig. S3).

3.4. An in vitro – in silico approach to study tortuous impact on oral mucosal permeation

We next developed an *in silico* model to capture the impact of extracellular convolutions on chemical permeation through TENOM. Data from *in vitro* human TENOM equivalents are used here because *ex vivo* NOM human tissue is minimally available for experiments and TENOM offers several advantages over use of porcine buccal mucosa. By incorporating measurements of extracellular space widths (Fig. 1L), cell geometry (Fig. 1N), epithelial layer thickness (Fig. 1O), and nuclei coordinates (Fig. 3B), the *in silico* model is geometrically comparable to the cellular histological structure of the buccal mucosa (Fig. 3A-D). Cell boundaries are deduced with a modified Voronoi tessellation in which the elongation of cells from the basal to the superficial layer is accounted for (Fig. 3C). Extracellular spaces have width w (Fig. 3D), equivalent to the measurements obtained in each epithelium strata (Table S3).

A schematic of the mathematical model is provided in Fig. 3E. Chemical transport through the spinosum and basal layers is modelled with diffusion in the extracellular spaces and intracellular regions (coefficients D_E and D_I) and permeability through cell membranes (coefficient Q). The extracellular spaces in this model are straight, but incorporate the established convoluted geometry, where extracellular diffusion is reduced by subcellular tortuosity τ_S (eqn. (1). A chemical is applied in an application layer with superficial and lamina propria layers included. At the base of the lamina propria, perfect sink conditions mimic a relatively large volume of receptive medium used in the tissue culture conditions when TENOM are used in these experiments

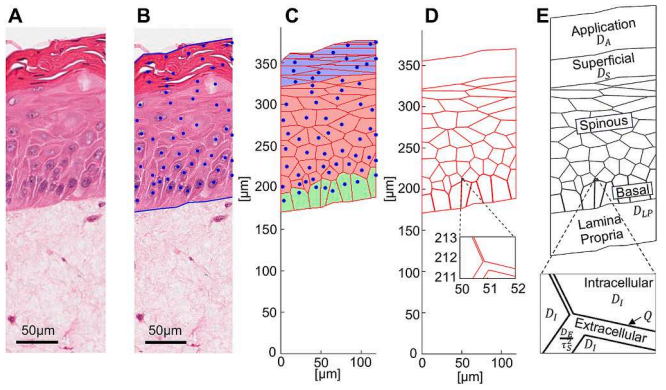

Fig. 3. *In silico* model development of chemical permeation through tissue-engineered normal oral mucosa. (A) Haematoxylin and eosin (H&E) stained tissue section of TENOM showing basal, spinous and superficial epithelial strata on top of the lamina propria. (B) Nuclei coordinates (blue dots), inferred from histological H&E staining of TENOM, are used to construct cell boundaries using (C) Voronoi tessellation where epithelial strata are identified as basal (green), spinous (red) and superficial (blue). (D) Extracellular spaces are imposed on the basal and spinous strata and the superficial layer is isolated. (E) Chemical permeation is modelled with diffusion (coefficient D) and membrane-permeability (coefficient Q). Diffusion in each region can differ: application D_A, superficial D_S, extracellular D_E, intracellular D_I, and lamina propria D_{LP}. Extracellular diffusion is slowed to account for subcellular tortuosity τ_S.

(Fig. 4A).

Oxymetazoline HCl (logP = 3.37), a small molecule vasoconstrictor that acts on blood vessels in the lamina propria, was topically applied in solution [3.4 mM] to the surface of TENOM (Fig. 4A) and the percentage permeation determined by measuring the concentration of oxymetazoline HCl in the receptive medium over time (Fig. 4B) by HPLC. After four hours, 53.6 ± 15.7 % of oxymetazoline HCL had permeated the TENOM, rising to 77.8 ± 20.0 % by six hours. The *in silico* model was fitted to this data. With diffusion coefficients in each layer already established (Table S4), fitting was undertaken using Newton iteration in the membrane permeability parameter Q and we deduced $Q = 4.74 \times 10^{-7}$ ms^{-1} for oxymetazoline HCl. Predicted oxymetazoline HCl concentrations throughout the entire TENOM epithelium are given in Fig. 4C over 360 min, alongside magnifications of the epithelium (Fig. 4D) and the extracellular space (Fig. 4E) at 30 min. Corresponding videos of Fig. 4C are provided in Fig. S4.

The *in silico* model was used to predict permeation for additional chemicals with different physiochemical properties. In Fig. 5, the chemicals' percentage permeation and magnifications of the epithelium in the upper spinous strata are presented. Biochemical properties and model parameters are provided in Table S4. A highly membrane-permeating chemical (hypothetical chemical X), which otherwise has the same biochemical properties as oxymetazoline HCl, is predicted to permeate much quicker (50 % permeated at 24.5 min, Fig. 5A). As diffusion coefficients vary minimally between small molecule drugs, this is approximately the minimum time a chemical can permeate TENOM. In this example, the chemical concentration is almost identical in the extracellular and intracellular spaces (Fig. 5B), implying that cellular

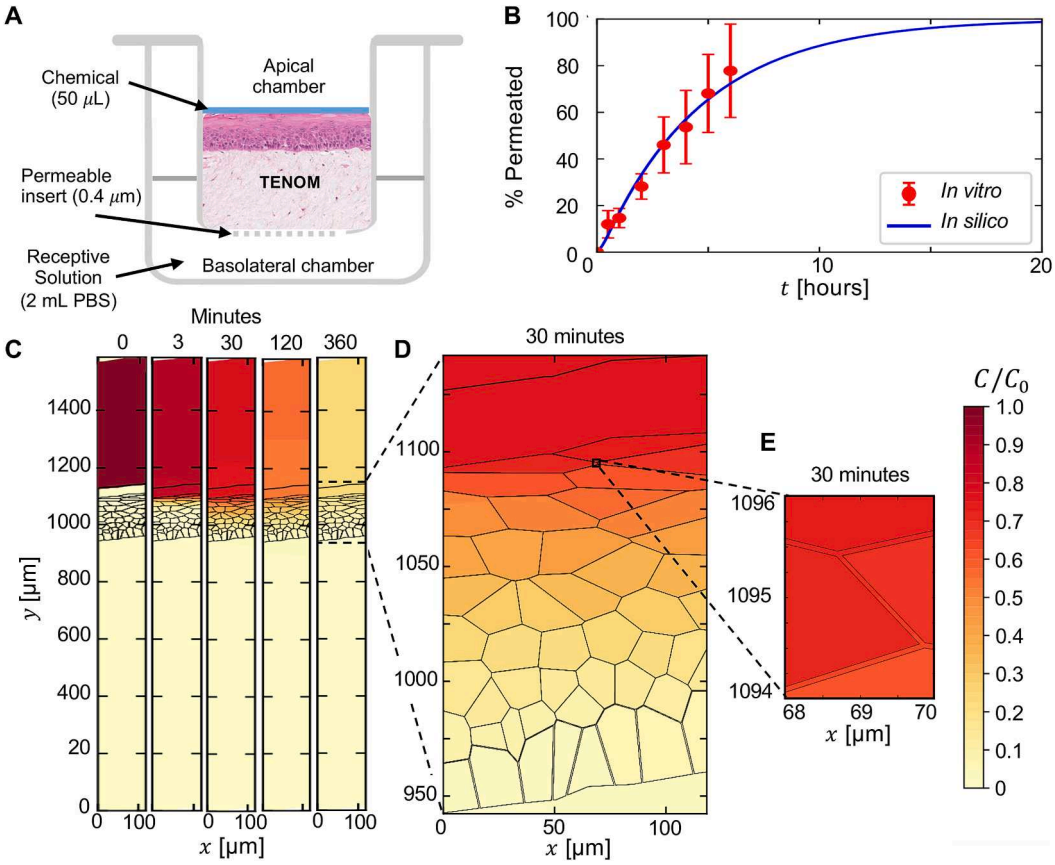

Fig. 4. Permeation of oxymetazoline HCl through tissue-engineered normal oral mucosa modelled *in vitro* and *in silico*. (A) *In vitro* permeation assay with 50 μl of oxymetazoline HCl (concentration $C_0 = 3.4$ mM) applied to a 113.1 mm^2 transwell surface (2 mL PBS in basolateral chamber as sink). (B) *In vitro* permeation data (mean ± SD) is captured *in silico* by fitting chemical membrane-permeability ($Q = 4.74 \times 10^{-7}$ ms^{-1}). (C) Predicted oxymetazoline HCl concentrations C over 360 min by the *in silico* model in the whole tissue. (D) Magnification of the entire epithelium strata and (E) magnification of the extracellular spaces in the upper spinous strata.

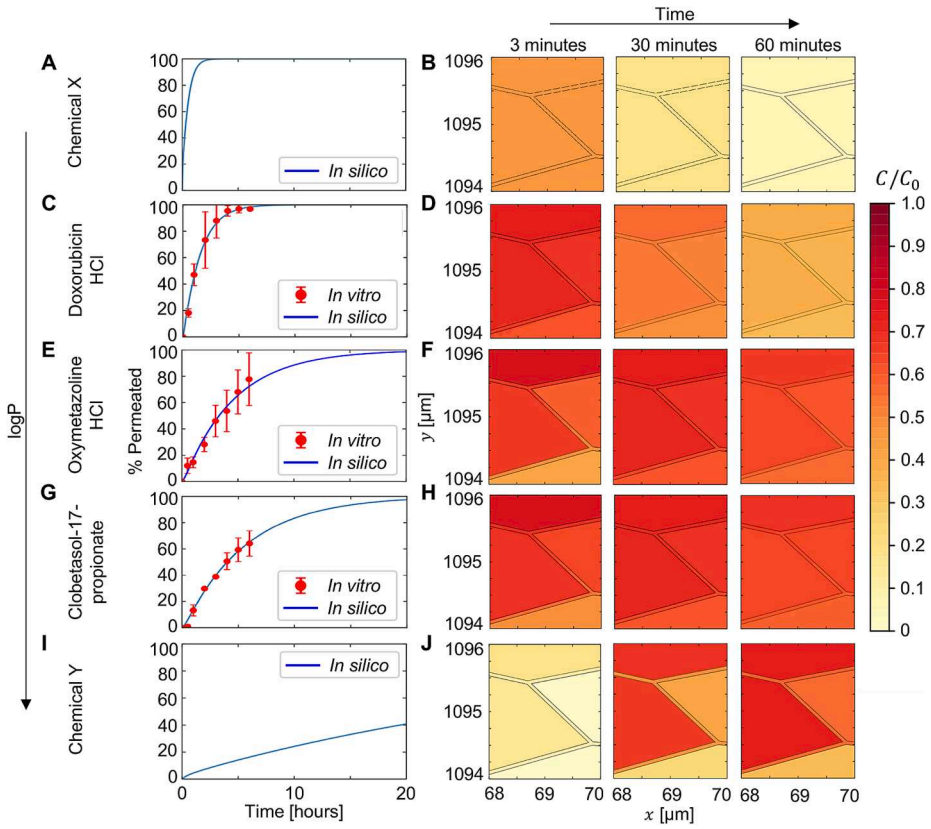

Fig. 5. Permeation of multiple chemicals through TENOM and corresponding extracellular and intracellular predictions modelled *in silico*. (A,C,E,G,I) *In vitro* permeation of doxorubicin HCl (logP = 0.97, $Q = 2.13 \times 10^{-6}$ ms^{-1}), oxymetazoline HCl (logP = 3.37, $Q = 4.74 \times 10^{-7}$ ms^{-1}), and clobetasol-17-propionate (logP = 3.84, $Q = 3.96 \times 10^{-7}$ ms^{-1}) is captured by the *in silico* model on fitting membrane permeability. The permeation of chemicals X and Y, with the same physiochemical properties as oxymetazoline HCl except with high ($Q = 10^{-3}$ ms^{-1}) or low ($Q = 10^{-8}$ ms^{-1}) membrane-permeablility respectively, is also predicted *in silico*. (B,D,F,H,J) Predicted extracellular and intracellular concentrations C/C_0 in the upper spinous strata of each chemical at 3, 30 and 60 min.

geometry has minimal effect on chemical permeation. *In vitro* experiments were also undertaken and fitted for doxorubicin HCl, a chemotherapeutic drug, and clobetasol-17-propionate, an immune-modulating corticosteroid. The time for these chemicals to permeate TENOM increases in a logP-dependent manner: doxorubicin HCl (logP = 0.97, 50 % at 1.12 h, Fig. 5C-D), followed by oxymetazoline HCl (logP = 3.37, 50 % at 3.65 h, Fig. 5E-F), and finally clobetasol-17-propionate (logP = 3.84, 50 % at 4.02 h, Fig. 5G-H). Similar to chemical X, the predicted extracellular and intracellular concentrations of doxorubicin HCl are almost identical (Fig. 5D), suggesting transcellular permeation. The distinction between paracellular and transcellular permeation becomes apparent for oxymetazoline HCl (Fig. 5F) and clobetasol-17-propionate (Fig. 5H) as lipophilicity increases. This is most apparent for highly lipophilic, poorly membrane-permeating chemicals such as hypothetical chemical Y (Fig. 5I-J), which otherwise has the same biochemical properties as oxymetazoline HCl.

Chemical permeation through TENOM epithelium at tissue scale is presented for each chemical in Fig. 6. Highly membrane-permeable chemical X is uniformly distributed throughout the epithelium, with no variation due to cellular geometry, suggesting rapid transcellular permeation (Fig. 6A). Doxorubicin HCl (Fig. 6B) has a concentration gradient through the epithelium, but the cellular geometry continues to be unimportant. However, the tissue architecture starts to have a much greater impact as lipophilicity increases. Here, the ability for these chemicals to penetrate epithelial cells decreases, as evidenced by oxymetazoline HCl (Fig. 6C), clobetasol-17-propionate (Fig. 6D) and highly lipophilic chemical Y (Fig. 6E). Chemical Y is restricted to cells in the superficial and upper spinous strata; however it does permeate (Fig. 5I), suggesting that the paracellular route dominates for highly lipophillic drugs.

In Fig. 7 the extracellular space is adjusted to mimic the actions of permeation enhancing chemicals that can alter the geometry of the paracellular space. Permeation for doxorubicin HCl (Fig. 7A) is only minimally affected by changes to the extracellular space geometry. However, the effects of permeation enhancers on the convoluted extracellular space are important for less permeable chemicals like oxymetazoline HCl (Fig. 7B) and clobetasol-17-priopionate (Fig. 7C) that permeate paracellularly. Widening the extracellular space alone has minimal effect on overall permeation; but straightened gaps display enhanced permeation (50 % at 2.53 h for oxymetazoline HCl), which is substantially increased with extracellular space widening (50 % at 1.07 h for oxymetazoline HCl).

4. Discussion

Administration of drugs/chemicals via the oral buccal mucosa provides several clinical and pharmacokinetic advantages that can positively impact patient pharmacotherapy, including avoiding stomach acid, circumventing hepatic first-pass clearance, and its suitability for chemically unstable and sensitive substances (Brandl and Bauer-Brandl, 2019; Zhang et al., 2002). Generally, rodents are the animal of choice for *in vivo* drug delivery or chemical toxicity studies but their usefulness for transbuccal studies is highly questionable as the structure of their oral mucosa is vastly different to humans. Rodent oral mucosa is keratinized and impermeable at the surface, resembling skin rather than the non-keratinized, permeable epithelium that is present in many areas of the human oral cavity (Sa et al., 2016; Sattar et al., 2014). Moreover, there is insufficient tissue post-extraction for use in permeation assays. Post-

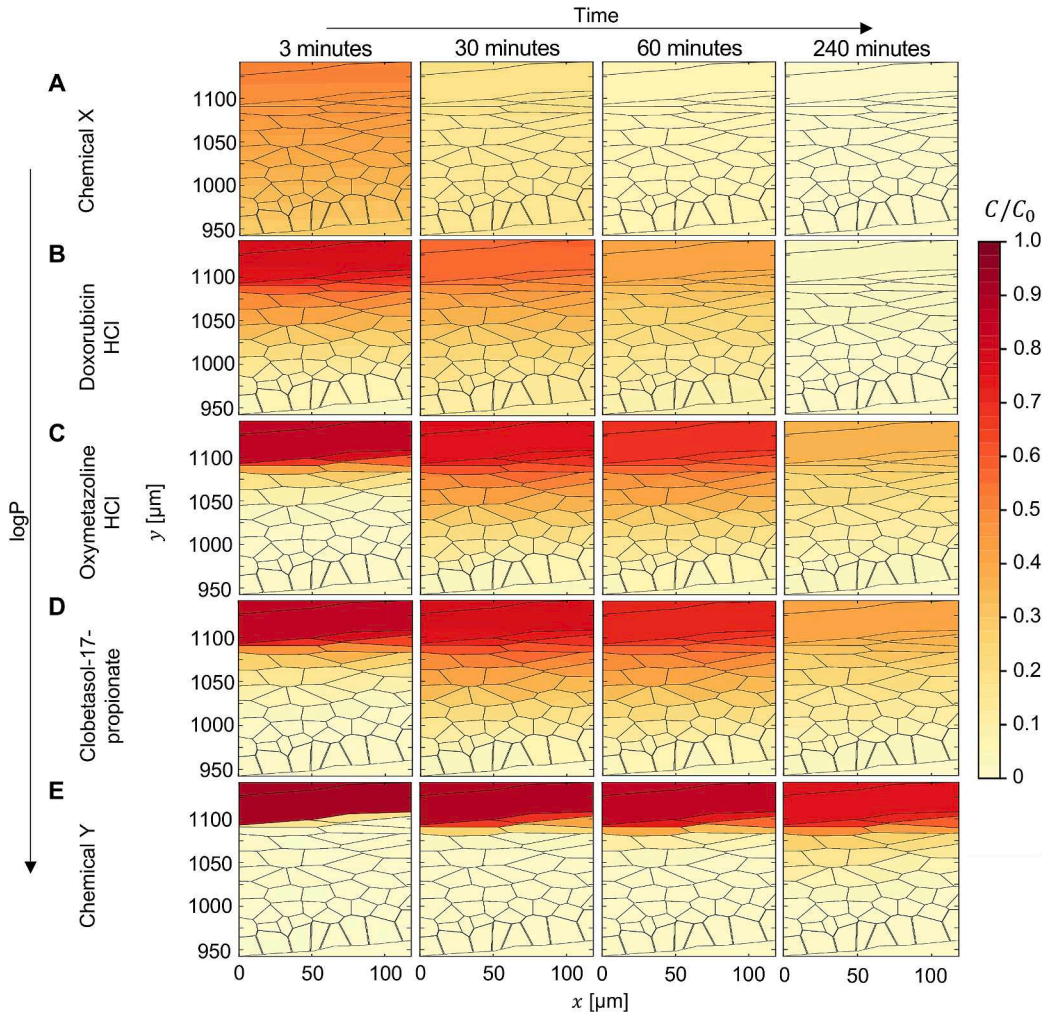

Fig. 6. Epithelial chemical concentration C/C_0 at 3, 30, 60 and 240 min predicted *in silico* for multiple chemicals: (A) highly membrane-permeable chemical X, (B) doxorubicin HCl, (C) oxymetazoline HCl, (D) clobetasol-17-propionate and (E) poorly membrane-permeable chemical Y.

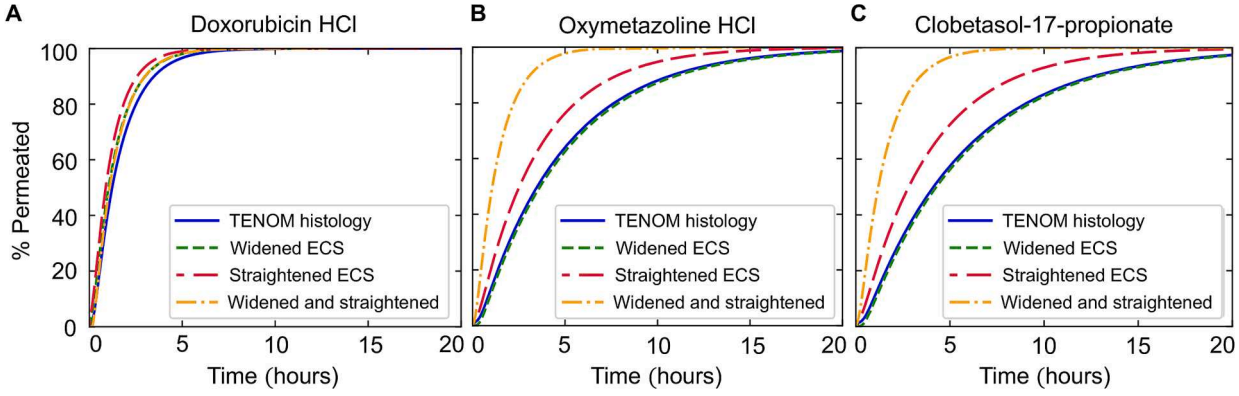

Fig. 7. Perturbation of extracellular space (ECS) geometry on the microscale can affect overall tissue permeation. The extracellular space (ECS) is widened ($w = 1\mu$ m), straightened ($\tau_S = 1$), and both by perturbing the *in silico* model. Doxorubicin HCl (A) is minimaly affected by the ECS geometry, but oxymetazoline HCl (B) and clobetasol-17-propionate (C) are predicted to permeate more quickly with wider, straightened ECS.

surgical *ex vivo* human oral mucosa is minimally available for laboratory experimentation (Sattar et al., 2014) therefore, in many instances, porcine buccal mucosa is used because it is structurally similar to human buccal tissue (Sa et al., 2016). However, these authors also note key features where porcine buccal mucosa differs from human tissue, such as in the thickness of the epithelium, in expression of cytokeratin markers and in basal cell proliferation (Sa et al 2016) that may or may not affect chemical permeation, and like humans, there are also concerns over pig-to-pig data variability (Kulkarni et al 2009).

Tissue engineered *in vitro* human buccal models also display very similar histological structure and express all the key markers compared to human buccal mucosa (Buskermolen et al., 2016; Gibbs and Ponec,

2000; Jennings et al., 2016; Said et al., 2021). Tissue engineered human buccal mucosal models can be produced upon demand, are relatively easy to construct and maintain in culture, have been extensively validated and are commercially available. Moreover, several studies have shown that tissue engineered buccal models display very similar drug permeation to porcine buccal mucosa for a number of chemicals (Boateng and Okeke, 2019; De Caro et al., 2008; Giannola et al., 2007; Rai et al., 2011). Permeation assays using TENOM have the potential to reduce animal burden and expedite the screening process for novel chemical compounds. However, a difference does occur with the relative size of the spinous layer between NOM and TENOM. With the future aim to extrapolate *in vitro* drug permeation results to *in vivo*, this difference can be factored in to the *in silico* model that incorporates all the other measured tissue geometries.

In silico models are now firmly recognised as an effective approach for experimental extrapolation and outcome prediction of tissue permeation (Anissimov et al., 2013) but their transferability to clinical or regulatory use is highly dependent on the data used and the approximations made. To date, the information available on the permeability of chemicals across epithelia largely originate from skin, whereby several mathematical models have been developed using skin-specific data to predict transdermal chemical permeability (Tsakovska et al., 2017). Indeed, mathematical models of the oral mucosa are very sparse (Goswami et al., 2013; Kokate et al., 2009; Xia, 2015). The buccal mucosa displays several distinct features (non-keratinized, thicker epithelium with increased permeability), making it dissimilar to skin. Since these features predominantly determine the rate-limiting step for transepithelial drug delivery, mathematical models developed to predict drug delivery across the skin are not entirely applicable to that of the oral mucosa, warranting separate investigations of oral mucosal-specific parameters that has driven the necessity for this research.

Similar to many other tissues (e.g., skin (Vela-Romera et al., 2019), liver (Ghadially and Parry, 1966), brain (Sykova, 2021), vaginal mucosa (Raudrant et al., 1989)), buccal mucosa exhibits convoluted extracellular spaces, and since many chemicals permeate tissue via this paracellular route, these spaces may significantly impact permeation. Whilst the impact of cell-scale tortuosity due to differing cell sizes and shapes has been considered before (Leedale et al., 2020), subcellular convoluted geometries have been largely ignored. For the first time, the influence of convoluted extracellular space on drug permeation has been elucidated. Membrane-impermeable chemicals that are restricted to the paracellular route are significantly slowed as they pass through the convoluted extracellular space. However, increased cellular surface areas improve transcellular permeation for moderately membrane-permeable chemicals. These contrasting effects depend on the physicochemical properties of the administered chemical and accounting for these is particularly important for low membrane-permeating chemicals. We have shown that our *in silico* model can account for the convoluted geometries by appropriately reducing extracellular diffusion, making a significant advancement in this area of research.

This study introduces an innovative whole-epithelium *in silico* model describing the marked impact that extracellular spaces of the oral mucosa have on drug permeation. Employing buccal tissue and cell geometry measurements, our model surpasses existing alternatives in its sophistication and accuracy. Crucially, by using partial differential equations, physiochemical permeation dynamics are included, such as extracellular and intracellular diffusion and permeation of cell membranes, along with real cell-shapes, cell-sizes and convoluted extracellular spaces; a significant improvement on previous models. The model captures permeation of chemicals over a range of lipophilicity, and can simultaneously account for transcellular and paracellular permeation. The tissue architecture can also be directly perturbed in the model. If the convoluted subcellular geometry is ignored, lipophilic chemicals are improperly accounted for and, for example, the time of oxymetazoline HCl to reach 50 % permeation is underpredicted by 30 %. Prediction of permeation for chemicals with different physicochemical properties, with lipophilicity being a key determining factor, may be even more inaccurate. This discrepancy in predictive power may have significant implications for investigators aiming to understand the kinetics of drug delivery to the oral mucosa, drug availability within epithelial tissue or maintaining clinically-relevant levels of drugs over specific periods of time.

Permeation can also be improved if the extracellular space is enlarged, for example with tissue permeation enhancers (Bzik and Brayden, 2016; Sohi et al., 2010), the modelling of which is crucial if chemical permeation through tissues is to be improved to expediate systemic delivery. Our model predicts that membrane-permeable (diffusion-limited) chemicals that permeate transcellularly are minimally affected by cellular geometry, while the opposite is true for low permeating chemicals. This feature will allow investigators to determine which permeation enhancers to select for a given chemical to fine tune its delivery.

5. Conclusion

Our combined *in vitro* – *in silico* approach has the potential to significantly improve oral pharmacokinetics and advance buccal-delivered therapies. Further action is needed to develop a comparative *in silico* model of *in vivo* tissue, in which chemicals pass to the bloodstream, parameterized by further *in vitro* permeation studies. Our *in silico* model could then be linked to physiologically-based pharmacokinetic (PBPK) models, allowing prediction of chemical distribution throughout the body. The methodology developed here also has the potential to impact wider drug distribution modelling, if adopted for other tissues and modalities, improving predictability while reducing the need for animal testing.

Author contribution statement

SME, ALH, JAL, SDW, HEC, CM and RNB conceptualized research and designed methodology; SME and ALH performed investigative research, validation and formal data analysis; SME designed, implemented and tested computer code; CM, RNB and HEC secured funding and supervised the project; CM had overall responsibility for project administration; SME, ALH prepared the draft writing of the manuscript; all authors reviewed and edited the manuscript

Declaration of competing interest

The authors declare the following financial interests/personal relationships which may be considered as potential competing interests: [Craig Murdoch reports financial support, article publishing charges, and travel were provided by National Centre for the Replacement Refinement and Reduction of Animals in Research. Steve Webb and Joseph Leedale reports a relationship with Syngenta that includes: employment. If there are other authors, they declare that they have no known competing financial interests or personal relationships that could have appeared to influence the work reported in this paper].

Acknowledgments

The authors would like to thank Dr Rob Bolt (Sheffield Teaching Hospitals NHS Foundation Trust) for collection of human tissue, Prof Ali Khurram (University of Sheffield) for sourcing archival paraffin-wax embedded human oral mucosal tissue. We also appreciate the support of Mr Chris Hill of the Cryo-Electron Microscopy Facility, University of Sheffield for help with transmission electron microscopy. This work was supported by the National Centre for the Replacement, Reduction and Refinement of Animals in Research (NC3Rs) UK, [grant number NC/W001160-1].

Appendix A. Supplementary material

Supplementary data to this article can be found online at https://doi.org/10.1016/j.ijpharm.2024.124827.

Data availability

Data will be made available on request.

References

Amestoy, P.D.L., Koster, J., L'Excellent, J., 2001. A fully asynchronous multifrontal solver using distributed dynamic scheduling. SIAM J. Matrix Anal. Appl. 23, 15–41.

Anissimov, Y.G., Jepps, O.G., Dancik, Y., Roberts, M.S., 2013. Mathematical and pharmacokinetic modelling of epidermal and dermal transport processes. Adv. Drug Deliv. Rev. 65, 169–190.

Balay, S.G.W., McInnes, L., Smith, B., 1997. Efficient management of parallelism in object oriented numerical software libraries. Modern Software Tools for Scientific Computing 163–202.

Bierbaumer, L., Schwarze, U.Y., Gruber, R., Neuhaus, W., 2018. Cell culture models of oral mucosal barriers: A review with a focus on applications, culture conditions and barrier properties. Tissue Barriers 6, 1479568.

Boateng, J., Okeke, O., 2019. Evaluation of clay-functionalized wafers and films for nicotine replacement therapy via buccal mucosa. Pharmaceutics 11.

Brandl, M., Bauer-Brandl, A., 2019. Oromucosal drug delivery: Trends in in-vitro biopharmaceutical assessment of new chemical entities and formulations. Eur. J. Pharm. Sci. 128, 112–117.

Brennan, M.T., Madsen, L.S., Saunders, D.P., Napenas, J.J., McCreary, C., Ni Riordain, R., Pedersen, A.M.L., Fedele, S., Cook, R.J., Abdelsayed, R., Llopiz, M.T., Sankar, V., Ryan, K., Culton, D.A., Akhlef, Y., Castillo, F., Fernandez, I., Jurge, S., Kerr, A.R., McDuffie, C., McGaw, T., Mighell, A., Sollecito, T.P., Schlieve, T., Carrozzo, M., Papas, A., Bengtsson, T., Al-Hashimi, I., Burke, L., Burkhart, N.W., Culshaw, S., Desai, B., Hansen, J., Jensen, P., Menne, T., Patel, P.B., Thornhill, M., Treister, N., Ruzicka, T., 2022. Efficacy and safety of a novel mucoadhesive clobetasol patch for treatment of erosive oral lichen planus: A phase 2 randomized clinical trial. J. Oral Pathol. Med. 51, 86–97.

Buskermolen, J.K., Reijnders, C.M., Spiekstra, S.W., Steinberg, T., Kleverlaan, C.J., Feilzer, A.J., Bakker, A.D., Gibbs, S., 2016. Development of a full-thickness human gingiva equivalent constructed from immortalized keratinocytes and fibroblasts. Tissue Eng. Part C Methods 22, 781–791.

Bzik, V.A., Brayden, D.J., 2016. An assessment of the permeation enhancer, 1-phenyl-piperazine (PPZ), on paracellular flux across rat intestinal mucosae in ussing chambers. Pharm. Res. 33, 2506–2516.

Chen, L., Han, L., Saib, O., Lian, G., 2015. In silico prediction of percutaneous absorption and disposition kinetics of chemicals. Pharm. Res. 32, 1779–1793.

Chen, J.Y.G., Yang, M., 2019. Computation of compact distributions of discrete elements. Algorithms 12, 41.

Colley, H.E., Hearnden, V., Jones, A.V., Weinreb, P.H., Violette, S.M., Macneil, S., Thornhill, M.H., Murdoch, C., 2011. Development of tissue-engineered models of oral dysplasia and early invasive oral squamous cell carcinoma. Br. J. Cancer 105, 1582–1592.

Colley, H.E., Said, Z., Santocildes-Romero, M.E., Baker, S.R., D'Apice, K., Hansen, J., Madsen, L.S., Thornhill, M.H., Hatton, P.V., Murdoch, C., 2018. Pre-clinical evaluation of novel mucoadhesive bilayer patches for local delivery of clobetasol-17-propionate to the oral mucosa. Biomaterials 178, 134–146.

De Caro, V., Giandalia, G., Siragusa, M.G., Paderni, C., Campisi, G., Giannola, L.I., 2008. Evaluation of galantamine transbuccal absorption by reconstituted human oral epithelium and porcine tissue as buccal mucosa models: part I. Eur. J. Pharm. Biopharm. 70, 869–873.

Edmans, J.G., Clitherow, K.H., Murdoch, C., Hatton, P.V., Spain, S.G., Colley, H.E., 2020. Mucoadhesive electrospun fibre-based technologies for oral medicine. Pharmaceutics 12.

Ghadially, F.N., Parry, E.W., 1966. Ultrastructure of a human hepatocellular carcinoma and surrounding non-neoplastic liver. Cancer 19, 1989–2004.

Giannola, L.I., De Caro, V., Giandalia, G., Siragusa, M.G., Tripodo, C., Florena, A.M., Campisi, G., 2007. Release of naltrexone on buccal mucosa: permeation studies, histological aspects and matrix system design. Eur. J. Pharm. Biopharm. 67, 425–433.

Gibbs, S., Ponec, M., 2000. Intrinsic regulation of differentiation markers in human epidermis, hard palate and buccal mucosa. Arch. Oral Biol. 45, 149–158.

Goswami, T., Kokate, A., Jasti, B.R., Li, X., 2013. In silico model of drug permeability across sublingual mucosa. Arch. Oral Biol. 58, 545–551.

Hearnden, V., Sankar, V., Hull, K., Juras, D.V., Greenberg, M., Kerr, A.R., Lockhart, P.B., Patton, L.L., Porter, S., Thornhill, M.H., 2012. New developments and opportunities in oral mucosal drug delivery for local and systemic disease. Adv. Drug Deliv. Rev. 64, 16–28.

Ibrahim, S.S., Ragy, N.I., Nagy, N.A., El-Kammar, H., Elbakry, A.M., Ezzatt, O.M., 2023. Evaluation of muco-adhesive tacrolimus patch on caspase-3 induced apoptosis in oral lichen planus: a randomized clinical trial. BMC Oral Health 23, 99.

Jennings, L.R., Colley, H.E., Ong, J., Panagakos, F., Masters, J.G., Trivedi, H.M., Murdoch, C., Whawell, S., 2016. Development and characterization of in vitro human oral mucosal equivalents derived from immortalized oral keratinocytes. Tissue Eng. Part C Methods 22, 1108–1117.

Kaliman, S., Jayachandran, C., Rehfeldt, F., Smith, A.S., 2016. Limits of applicability of the voronoi tessellation determined by centers of cell nuclei to epithelium morphology. Front. Physiol. 7, 551.

Kinikoglu, B., Damour, O., Hasirci, V., 2015. Tissue engineering of oral mucosa: a shared concept with skin. J. Artif. Organs 18, 8–19.

Klausner, M., Handa, Y., Aizawa, S., 2021. In vitro three-dimensional organotypic culture models of the oral mucosa. In Vitro Cell. Dev. Biol. Anim. 57, 148–159.

Kokate, A., Li, X., Williams, P.J., Singh, P., Jasti, B.R., 2009. In silico prediction of drug permeability across buccal mucosa. Pharm. Res. 26, 1130–1139.

Kruse, J., Golden, D., Wilkinson, S., Williams, F., Kezic, S., Corish, J., 2007. Analysis, interpretation, and extrapolation of dermal permeation data using diffusion-based mathematical models. J. Pharm. Sci. 96, 682–703.

Kwapiszewska, K., Szczepanski, K., Kalwarczyk, T., Michalska, B., Patalas-Krawczyk, P., Szymanski, J., Andryszewski, T., Iwan, M., Duszynski, J., Holyst, R., 2020. Nanoscale viscosity of cytoplasm is conserved in human cell lines. J. Phys. Chem. Lett. 11, 6914–6920.

Leedale, J.A., Kyffin, J.A., Harding, A.L., Colley, H.E., Murdoch, C., Sharma, P., Williams, D.P., Webb, S.D., Bearon, R.N., 2020. Multiscale modelling of drug transport and metabolism in liver spheroids. Interface Focus 10, 20190041.

Lemke, S.B., Nelson, C.M., 2021. Dynamic changes in epithelial cell packing during tissue morphogenesis. Curr. Biol. 31, R1098–R1110.

McGregor, F., Muntoni, A., Fleming, J., Brown, J., Felix, D.H., MacDonald, D.G., Parkinson, E.K., Harrison, P.R., 2002. Molecular changes associated with oral dysplasia progression and acquisition of immortality: potential for its reversal by 5-azacytidine. Cancer Res. 62, 4757–4766.

Miller, C.C., 1924. The Stokes-Einstein law for diffusion in solution. Proceedings of the Royal Society of London. Series A, Containing Papers of a Mathematical and Physical Character 106, 724-749.

Moharamzadeh, K., Colley, H., Murdoch, C., Hearnden, V., Chai, W.L., Brook, I.M., Thornhill, M.H., Macneil, S., 2012. Tissue-engineered oral mucosa. J. Dent. Res. 91, 642–650.

Polak, S., Ghobadi, C., Mishra, H., Ahamadi, M., Patel, N., Jamei, M., Rostami-Hodjegan, A., 2012. Prediction of concentration-time profile and its inter-individual variability following the dermal drug absorption. J. Pharm. Sci. 101, 2584–2595.

Rai, V., Tan, H.S., Michniak-Kohn, B., 2011. Effect of surfactants and pH on naltrexone (NTX) permeation across buccal mucosa. Int. J. Pharm. 411, 92–97.

Raudrant, D., Frappart, L., De Haas, P., Thoulon, J.M., Charvet, F., 1989. Study of the vaginal mucous membrane following tampon utilisation; aspect on colposcopy, scanning electron microscopy and transmission electron microscopy. Eur. J. Obstet. Gynecol. Reprod. Biol. 31, 53–65.

Sa, G., Xiong, X., Wu, T., Yang, J., He, S., Zhao, Y., 2016. Histological features of oral epithelium in seven animal species: As a reference for selecting animal models. Eur. J. Pharm. Sci. 81, 10–17.

Said, Z., Murdoch, C., Hansen, J., Siim Madsen, L., Colley, H.E., 2021. Corticosteroid delivery using oral mucosa equivalents for the treatment of inflammatory mucosal diseases. Eur. J. Oral Sci. 129, e12761.

Sattar, M., Sayed, O.M., Lane, M.E., 2014. Oral transmucosal drug delivery–current status and future prospects. Int. J. Pharm. 471, 498–506.

Shah, M.B.L., Ali, S., Al-Enazy, S., Youssef, M.M., Fisler, M., Rytting, E., 2018. HPLC method development for quantification of doxorubicin in cell culture and placental perfusion media. Separations 5, 9.

Sohi, H., Ahuja, A., Ahmad, F.J., Khar, R.K., 2010. Critical evaluation of permeation enhancers for oral mucosal drug delivery. Drug Dev. Ind. Pharm. 36, 254–282.

Stanisz, B., Nowinski, W., 2000. Determination of oxymetazoline hydrochloride and decomposition products by high-performance liquid chromatography. Acta Pol. Pharm. 57, 399–401.

Sykova, E.N.C., 2021. Diffusion in brain extracellular space. Physiol. Rev. 88, 1277–1340.

Targhotra, M., Chauhan, M.K., 2020. An overview on various approaches and recent patents on buccal drug delivery systems. Curr. Pharm. Des. 26, 5030–5039.

Tsakovska, I., Pajeva, I., Al Sharif, M., Alov, P., Fioravanzo, E., Kovarich, S., Worth, A.P., Richarz, A.N., Yang, C., Mostrag-Szlichtyng, A., Cronin, M.T.D., 2017. Quantitative structure-skin permeability relationships. Toxicology 387, 27–42.

Vela-Romera, A., Carriel, V., Martin-Piedra, M.A., Aneiros-Fernandez, J., Campos, F., Chato-Astrain, J., Prados-Olleta, N., Campos, A., Alaminos, M., Garzon, I., 2019. Characterization of the human ridged and non-ridged skin: a comprehensive histological, histochemical and immunohistochemical analysis. Histochem. Cell Biol. 151, 57–73.

Verma, L.G.K., Gupta, R., Rai, B., 2023. Multiscale modeling of molecule transport through skin's deeper layers. Comput. Toxicol. 26, 100267.

Xia, B.Y.Z., Zhou, H., Lukacova, V., Zhu, W., Milewski, M., Kesisoglou, F., 2015. Development of a novel oral cavity compartmental absorption and transit model for sublingual administration: illustration with zolpidem. AAPS J. 17, 631–642.

Zhang, H.Z.J., Streisand, J.B., 2002. Oral mucosal drug delivery: clinical pharmacokinetics and therapeutic applications. Clin. Pharmacokinet. 41, 661–680.

Zhou, Y., Wang, M., Yan, C., Liu, H., Yu, D.G., 2022. Advances in the application of electrospun drug-loaded nanofibers in the treatment of oral ulcers. Biomolecules 12.

An advanced *in silico* model of the oral mucosa reveals the impact of extracellular spaces on chemical permeation

Sean M. Edwards[a,§], Amy L. Harding[b,§], Joseph A. Leedale[c], Steve D. Webb[c], Helen E. Colley[b], Craig Murdoch[b,1,*]and Rachel N. Bearon[a,d,*]

Supplementary Information

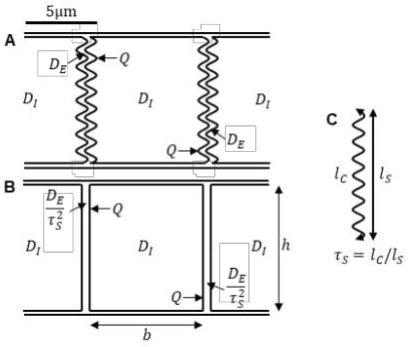

Supplemental figure 1. *In silico* schematic of chemical permeation through a normal oral mucosal (NOM) basal cell monolayer. Chemicals diffuse with coefficients D_E (extracellular), D_I (intracellular) and permeate cell membranes with rate Q (A). (B) A straight-gap approximation has reduced extracellular diffusion. (C) Subcellular tortuosity $\tau_S > 1$ is the length of a convoluted gap l_C relative to a straight gap l_S.

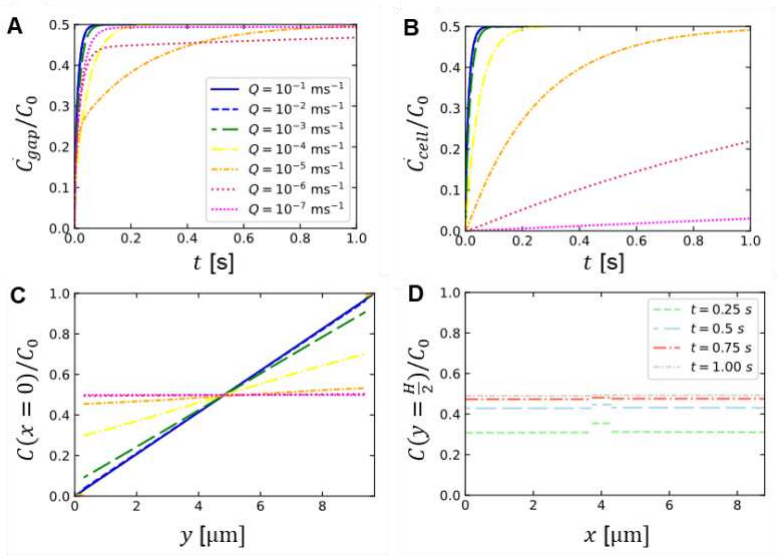

Supplemental figure 2. Effect of membrane permeability Q on constant-supply chemical permeation through a monolayer of oral basal cells. A constant supply (concentration C_0) of a test chemical (diffusion coefficients $D_E = D_I = 7.5 \times 10^{-10} m^2 s^{-1}$) is applied to the apical cell surface and up taken below the monolayer. (A, B) Average drug concentration $\bar{C}$ in the central extracellular space (A) and intracellularly (B). The legend in (A) also applies to (B, C). Highly membrane-permeable chemicals $Q > 10^{-3}$ ms^{-1} quickly reach a steady-state. Moderately permeable chemicals $10^{-6} < Q < 10^{-3}$ ms^{-1} take much longer to reach steady-state. Chemicals which are poorly membrane-permeable $Q < 10^{-6}$ms^{-1} reach steady-state quickly in the gaps but slowly in the cells. (C) The concentration C from the top to the bottom of the epithelium along the centre of cells (at $x = 0$) approaches a constant $C/C_0 = 1/2$ as the cell membrane permeability Q is decreased. (D) Along the middle of the epithelium (on $y = H/2$) the difference in concentration between the central extracellular space and the cells is apparent at varying timepoints for $Q = 10^{-5}$ ms^{-1}.

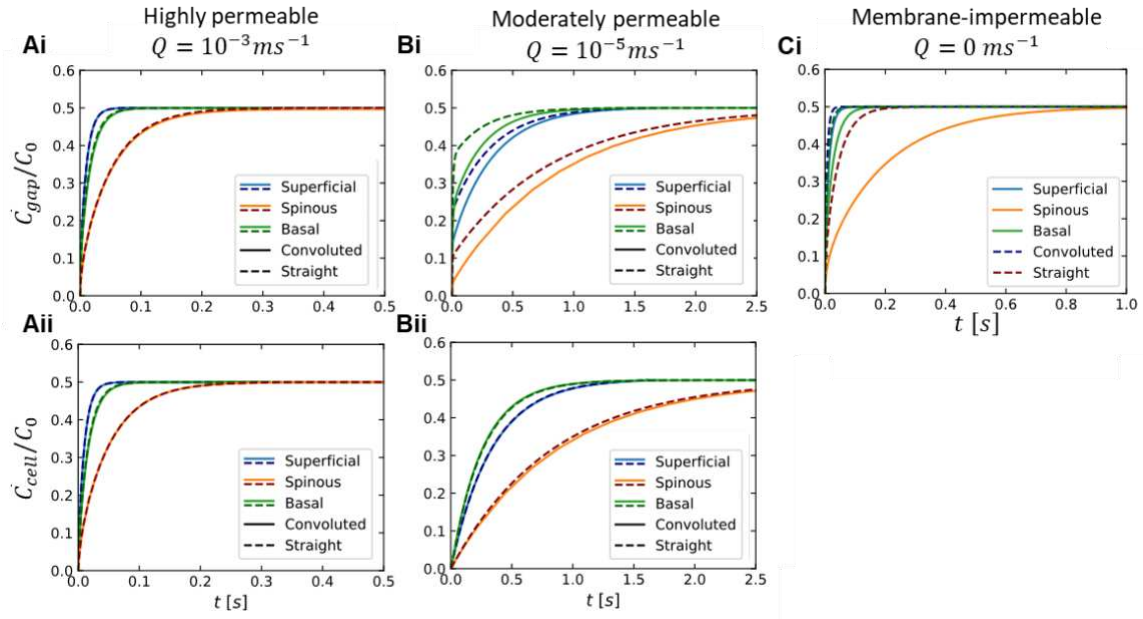

Supplemental figure 3. Chemical permeation through a monolayer of oral keratinocytes modelled *in silico*: convoluted extracellular space compared to straight extracellular space without subcellular tortuosity accounted for $\tau_S = 1$. Permeation through straight extracellular space is consistently quicker than in the physical convoluted model. However, by diminishing extracellular diffusion the straight-extracellular space model can provide a good approximation (see manuscript Fig. 2). Here a test chemical (diffusion coefficients $D_E = D_I = 7.5 \times 10^{-10} \mathrm{m^2 s^{-1}}$) permeates membranes with varying coefficients Q. A constant supply is applied with concentration C_0. Keratinocytes from each epithelial cell layer are modelled (superficial, spinous, basal) by incorporating physically relevant cell breadths, cell heights and convoluted extracellular space.

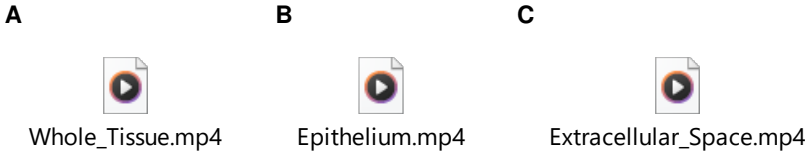

Supplemental figure 4. Epithelial concentration of oxymetazoline HCl predicted over time through TENOM by the *in silico* model (MP4 videos). Chemical concentration is shown through (A) the whole tissue, (B) the epithelium and (C) the extracellular space in the superficial layer. This figure pairs with manuscript Fig. 4C-E.

Supplemental Table 1. High performance liquid chromatography standards validation data. Correlation coefficient and regression statistics; limit of detection (LoD) and limit of quantification (LoQ) defined as the concentration of analytes with a signal-to-noise ratio of 3:1 and 10:1, respectively, and calculated using the following equations: LoD = (3.3σ/*s*) and LoQ= (10σ/*s*), where σ is the standard deviation of intercept and *s* is the slope of the calibration plot.

	Correlation Coefficient	Limit of Detection (μg/mL)	Limit of Quantification (μg/mL)
Oxymetazoline HCL	0.99	0.51	1.54
Doxorubicin-HCL	0.99	1.49	4.50
Clobetasol-17-propionate	0.99	1.45	4.38

Supplemental Table 2. Calculated tortuosity at each scale: subcellular, cellular and whole epithelial. Convoluted extracellular spaces are assumed sinusoidal on a subcellular scale; subcellular tortuosity τ_S is the arclength of the space divided by the wavelength. Cell heights h and breadths b inform cellular tortuosity $\tau_C = (b+h)/h$ (disregarding subcellular convolutedness). Tortuosity $\tau = \tau_S\tau_C$ is then the overall extracellular pathlength relative to the thickness of each epithelial cell-layer.

		Basal	**Spinous**	**Superficial**
Subcellular tortuosity τ_S	NOM	1.881 ± 0.619	2.188 ± 0.607	1.891 ± 0.638
	TENOM	2.410 ± 0.663	3.576 ± 1.431	7.761 ± 4.694
Cellular tortuosity τ_C	NOM	1.903 ± 0.239	2.416 ± 1.506	6.149 ± 3.330
	TENOM	1.589 ± 0.393	2.824 ± 1.247	10.163 ± 3.027
Overall tortuosity τ	NOM	3.576 ± 0.663	5.286 ± 1.624	11.623 ± 3.391
	TENOM	3.830 ± 0.771	10.099 ± 1.898	78.875 ± 5.585

Supplemental Table 3. Measured geometries of normal oral mucosa (NOM) and tissue-engineered normal oral mucosa (TENOM) in epithelial strata (basal, spinous and superficial). Data are presented in order of scale: subcellular, cellular and epithelial strata. Convoluted extracellular space of width w are assumed sinusoidal on a subcellular scale with amplitude A and wavelength λ. Cell heights h and breadths b are measured in each stratum.

			Basal	**Spinous**	**Superficial**
Subcellular geometry	Gap width w [μm]	NOM	0.575 ± 0.329	0.102 ± 0.036	0.077 ± 0.050
		TENOM	0.640 ± 0.349	0.053 ± 0.021	0.048 ± 0.031
	Gap amplitude A [μm]	NOM	0.410 ± 0.122	0.299 ± 0.088	0.181 ± 0.089
		TENOM	0.590 ± 0.119	0.443 ± 0.138	0.560 ± 0.220
	Gap wavelength λ [μm]	NOM	1.059 ± 0.491	0.576 ± 0.137	0.455 ± 0.123
		TENOM	1.115 ± 0.312	0.527 ± 0.168	0.293 ± 0.141
Cellular geometry	Cell height h [μm]	NOM	9.11 ± 0.81	18.19 ± 6.69	7.13 ± 2.98
		TENOM	22.90 ± 3.86	16.79 ± 4.23	4.35 ± 1.28
	Cell breadth b [μm]	NOM	8.23 ± 0.73	25.75 ± 12.96	36.71 ± 12.64
		TENOM	13.49 ± 2.44	30.62 ± 11.10	39.86 ± 1.83
Epithelial cell-layer geometry	Cell-layer thickness [μm]	NOM	9.11 ± 0.81	499.30 ± 63.07	62.80 ± 15.59
		TENOM	22.90 ± 3.86	148.70 ± 21.61	33.67 ± 9.26

Supplemental Table 4. Biochemical properties*, in silico* model diffusion coefficients and membrane permeation parameters for each chemical. Extracellular diffusion coefficients were approximated to water; intracellular diffusion coefficients were predicted by the model suggested by Kwapiszewska *et al.* (36) for human epithelial cell lines; and for doxorubicin HCl, oxymetazoline HCl, and clobetasol-17-propionate membrane permeability parameters were Newton iterated to fit to *in vitro* permeation data. Chemicals X and Y have the same properties as oxymetazoline HCl except for lipophilicity (the membrane permeability parameter is modified). LogP values are the average of predictions made by ALOGPS 2.1 (37) and Chemaxon.

	Molecular mass M	**Density ρ [g cm^{-3}]**	**logP**	**Extracellular diffusion D_E [m^{2}s^{-1}]**	**Intracellular diffusion D_I [m^{2}s^{-1}]**	**Membrane permeability Q [ms^{-1}]**
Chemical X	296.84	1.10	low	6.922×10^{-10}	4.049×10^{-10}	1×10^{-3}
Doxorubicin HCl	579.98	1.61	0.97	6.287×10^{-10}	3.621×10^{-10}	2.134×10^{-6}
Oxymetazoline HCl	296.84	1.10	3.37	6.922×10^{-10}	4.049×10^{-10}	4.742×10^{-7}
Clobetasol-17-propionate	466.97	1.32	3.84	6.293×10^{-10}	3.624×10^{-10}	3.960×10^{-7}